Journal of Advanced Ceramics
2022, **11**(2): 295–307
https://doi.org/10.1007/s40145-021-0533-7
ISSN 2226-4108
CN 10-1154/TQ

Research Article

Novel 3D grid porous $Li_4Ti_5O_{12}$ thick electrodes fabricated by 3D printing for high performance lithium-ion batteries

Changyong LIU[a,b], Yin QIU[a], Yanliang LIU[a], Kun XU[a], Ning ZHAO[a], Changshi LAO[a], Jun SHEN[b], Zhangwei CHEN[a,b,*]

[a]*Additive Manufacturing Institute, College of Mechatronics & Control Engineering, Shenzhen University, Shenzhen 518060, China*
[b]*Guangdong Key Laboratory of Electromagnetic Control and Intelligent Robots, College of Mechatronics & Control Engineering, Shenzhen University, Shenzhen 518060, China*

Received: May 5, 2021; Revised: September 4, 2021; Accepted: September 4, 2021
© The Author(s) 2021.

Abstract: Three-dimensional (3D) grid porous electrodes introduce vertically aligned pores as a convenient path for the transport of lithium-ions (Li-ions), thereby reducing the total transport distance of Li-ions and improving the reaction kinetics. Although there have been other studies focusing on 3D electrodes fabricated by 3D printing, there still exists a gap between electrode design and their electrochemical performance. In this study, we try to bridge this gap through a comprehensive investigation on the effects of various electrode parameters including the electrode porosity, active material particle diameter, electrode electronic conductivity, electrode thickness, line width, and pore size on the electrochemical performance. Both numerical simulations and experimental investigations are conducted to systematically examine these effects. 3D grid porous $Li_4Ti_5O_{12}$ (LTO) thick electrodes are fabricated by low temperature direct writing technology and the electrodes with the thickness of 1085 μm and areal mass loading of 39.44 $mg \cdot cm^{-2}$ are obtained. The electrodes display impressive electrochemical performance with the areal capacity of 5.88 $mAh \cdot cm^{-2}$@1.0 C, areal energy density of 28.95 $J \cdot cm^{-2}$@1.0 C, and areal power density of 8.04 $mW \cdot cm^{-2}$@1.0 C. This study can provide design guidelines for obtaining 3D grid porous electrodes with superior electrochemical performance.

Keywords: three-dimensional (3D) porous thick electrodes; $Li_4Ti_5O_{12}$ (LTO); 3D printing; lithium-ion (Li-ion) battery

1 Introduction

Lithium-ion (Li-ion) batteries have been playing an indispensable role in modern society [1]. However, the urgent need for batteries with higher energy density and power density has always been a tremendous challenge. Commercial Li-ion batteries with thin coated electrodes face some intrinsic shortcomings [2]. For example, the total proportion of inactive materials including current collectors and separators can take over up to 50% of the total volume (excluding the encapsulation) [3]. However, only active materials contribute to energy storage; thereby it is highly desirable to maximize the

* Corresponding author.
E-mail: chen@szu.edu.cn

ratio of active materials and minimize the ratio of inactive active materials. In addition, for thin electrodes, the areal mass loading of active materials per footprint area is usually low due to the trade-off between energy density and power density [4–6].

Thick electrodes with the thickness of up to hundreds of microns can reduce the number of current collectors and separators at the cell level, thereby increasing the ratio of active materials as well as the mass loading of active materials per footprint area [4]. However, thick electrodes also face some critical challenges, especially the proportional increase of transport distance of electrons and Li-ions with the increase of electrode thickness [7]. The relatively poor charge transfer kinetics in thick electrodes requires longer time for electrons and Li-ions to reach the reaction sites and eventually lead to declined rate performance and energy density. Danner *et al*. [8] and Gao *et al*. [9] proposed theoretical and simulation models to study the rate limiting factors of thick NMC–graphite (Ni–Mn–Co ternary cathode and graphite anode) batteries with electrode thickness of 300 μm. It was found that the transport of Li-ions in the electrolyte phase is the major limiting factor. Therefore, improving the charge transfer kinetics is crucial for thick electrodes. Toward this end, simultaneously enhancing the effective electronic conductivity and effective ionic conductivity is a key step. However, how to fabricate thick electrodes with enhanced charge transfer kinetics remains a tremendous challenge. As for the transport of electrons, with more efficient percolation conductive network composed of highly conductive additives such as carbon nanotubes (CNTs) and graphene, it is relatively easy to achieve high electronic conductivity [10–12]. As for the transport of Li-ions in thick electrodes, it is very important to shorten the total transport distance of Li-ions so that the capacity at high charge/discharge rates can be maintained.

One of the approaches is to create directionally-ordered pores in the electrodes to reduce the tortuosity toward low tortuosity thick electrodes that are able to minimize the transport length of Li-ions in comparison with other non-directional pores. For example, Sander *et al*. [13] proposed a magnetic templating method that was able to magnetically align a sacrificial magnetic phase to obtain low tortuosity electrodes with aligned pores. Other structural templates such as natural wood and ice crystals have also been reported [14,15]. In addition, three-dimensional (3D) carbon frameworks made from CNTs, carbon nanofibers, and/or graphene nanosheets were also prepared as conductive 3D scaffolds for the loading of active materials to offer highly efficient charge delivery even in thick electrodes [4,5,16]. Although these approaches were able to construct low tortuosity thick electrodes through pore engineering strategies, the scalability of these processes is generally limited; therefore, scalable yet cost-effective processes are still needed [3].

3D printing has the capability of fabricating objects with unparalleled complex shapes and geometries; thereby it has been demonstrated as a powerful tool to fabricate thick electrodes with tailored 3D architectures [17–26]. There are many types of 3D printing technologies including materials extrusion, vat polymerization, powder bed fusion, direct energy deposition, and sheet lamination [18]. Direct ink writing (DIW) is a material extrusion process that extrudes inks from nozzles to fabricated 3D object in a layer upon layer fashion. Due to its simplicity and convenience of processing composite inks, it has been the most widely used technology in the fabrication of 3D Li-ion batteries. For example, Sun *et al*. [27] fabricated 3D micro-batteries with interdigitated $LiFePO_4$ (LFP) and $Li_4Ti_5O_{12}$ (LTO) electrodes and the electrode thickness was up to ~800 μm. In addition, graphene oxide-based electrodes [28], $LiMn_{1-x}Fe_xO_4$ cathodes [29], $LiCoO_2$ electrodes [30], $LiMn_2O_4$ electrodes [31], and all-fiber Li-ion batteries [32], etc., have also been fabricated by DIW [33–53]. These studies mainly focused on the ink preparation, rheological properties, and electrochemical characterization. However, the design principles and guidelines toward high performance 3D-printed thick electrodes are yet to be established.

LTO is a promising anode material that has been selected as the candidate for 3D-printed Li-ion batteries due to its nearly zero volume change during the charging and discharging process [53,54]. In this study, a comprehensive investigation on the effects of various electrode parameters including the electrode porosity, active materials' particle diameter, electronic conductivity, electrode thickness, line width, and pore size on electrochemical performance were conducted for 3D grid porous LTO electrodes. Firstly, the structure and charge delivery mechanism of 3D grid porous electrodes were discussed. Then a numerical simulation model was established to systematically examine these effects. After that, we fabricated 3D grid porous LTO electrodes via a low temperature direct writing-based 3D printing

technology. The microstructure, porosity, pore size and distribution, mechanical integrity, and electrochemical performance of 3D-printed LTO electrode half-cell with Li-foil as the counter electrode were then characterized. Combining the simulation results and experimental results, the relationship between the electrode parameters and electrochemical performance was established. Then the design guidelines for obtaining 3D grid porous electrodes with superior performance were discussed. This study can provide a deep understanding of the strength and weakness of 3D grid porous electrodes.

2 3D grid porous electrode and its charge delivery mechanism

The 3D Li-ion battery composed of 3D grid porous electrodes is shown in Figs. 1(a) and 1(b). 3D grid porous electrode is a type of thick electrodes that introduce vertically aligned pores as paths for the transport of Li-ions. In thin electrodes, Li-ions only need to penetrate through a thin layer with the thickness of tens of microns (Fig. 1(c)). While in thick electrodes, the electrode thickness increases up to hundreds of microns as shown in Fig. 1(d). With 3D grid porous electrodes, Li-ions can transport through the vertically aligned pores instead of the tortuous paths inside the electrodes, thereby reducing the total transport distance of Li-ions.

In 3D grid porous electrodes, the charge delivery mechanism is shown in Fig. S1 in the Electronic Supplementary Material (ESM). For the delivery of Li-ions, there are two major steps: the transport in solid phase (inside the active material particles) and the transport in liquid phase (inside the electrolyte). The active material particle diameter d and the bulk ionic conductivity are the major factors that impact the transport in solid phase. Usually, the active material particle diameter ranges from hundreds of nanometers to 10 μm. The smaller the diameter is, the faster the ions travel in solid phase and the better electrochemical performance at high charge/discharge rates will be. While for ionic transport in liquid phase, bulk ionic conductivity of electrolyte σ_{Li^+} and the total transport distance L are the major influencing factors. The total transport distance of Li-ions is determined by several factors including the electrode tortuosity τ, the electrode thickness, and the electrode structure. The vertically aligned pores in 3D grid porous electrodes can help to reduce the total transport distance and eventually improve the electrochemical performance of thick electrodes. While inside the porous electrodes, τ is a crucial factor and this value can be tailored by porosity ε. Reducing τ by increasing ε can help to reduce total ionic transport distance. Here, the ε refers to the internal ε of the electrode and does not include the macro-pores formed by the space between active material lines.

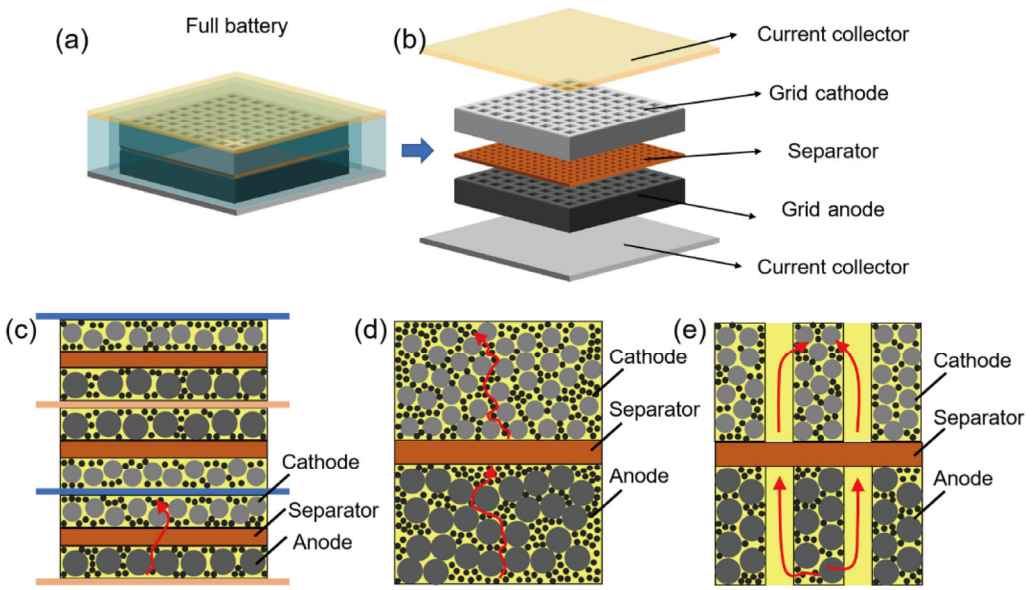

Fig. 1 Schematic of 3D Li-ion battery and its charge delivery mechanism: (a) 3D Li-ion battery based on 3D grid porous electrodes, (b) exploded view, (c) charge delivery in thin electrodes, (d) charge delivery in thick electrodes, and (e) charge delivery in 3D grid porous electrodes.

As for the transport of electrons, the total transport distance of electrons L' and electronic conductivity σ_e are the major influencing factors. Usually, electrons are transported through an electrically conductive percolation network composed of carbon additives. For thick electrodes, it is very important to ensure that the electrodes have excellent electronic conductivity. With more carbon additives involved, a higher electronic conductivity will be reached. However, a large ratio of carbon conductive agents means decreased ratio of active materials and is harmful to energy density. Therefore, it is highly desirable to construct an effective conductive network with the least amount of carbon additives.

To sum up, the transport of ions and electrons is influenced by many factors including geometrical parameters, microstructural parameters, and active material properties. To eventually obtain 3D grid porous thick electrodes with excellent electrochemical performance, it requires a comprehensive understanding of the relationship between these influencing factors and electrochemical performance.

3 Numerical simulations

3. 1 Model description

The geometry of 3D grid porous electrodes is shown in Fig. S2 in the ESM. The major geometrical parameters include: electrode thickness h, electrode width w, line spacing s, line width s_l, and pore size s_p. Among these parameters, line spacing equals to the sum of line width and pore size: $s = s_l + s_p$. To study the relationship between various electrode parameters and electrochemical performance of 3D grid porous electrodes, a numerical model based on COMSOL Multiphysics was set up. Since 3D grid porous electrodes have a periodic structure, it can be simplified with a two-dimensional (2D) half-cell model with Li-foil as counter electrode (Fig. S3 in the ESM). The reasonablility of the simplification of the model is described in more details in the ESM. In this study, we selected an anode material LTO as the active material and the process of discharge was simulated with a discharge cut-off voltage of 1.0 V.

Firstly, we start with the case using the parameters shown in Table S1 in the ESM. These parameters were determined based on commercial Li-ion battery configuration. The electrode thickness h was 0.3 mm and the value was approximately 10 times of conventional thin electrodes. The line width s_l was 0.25 mm and macro-pore size s_p was 0.1 mm. The volume fraction of active material φ_{act}, sub-material φ_{sub} (conductive agents and binders), and ε (excluding the space between active material lines) was 40%, 15%, and 45%, respectively, and $\varphi_{act} + \varphi_{sub} + \varepsilon = 1$. The particle diameter of active material d was 10 μm and σ_e was 100 $S \cdot m^{-1}$.

3. 2 Results and discussion

Figure 2 shows the comparison of 0.3 mm thick planar electrodes without vertical path and 0.3 mm thick 3D grid porous electrodes with vertical path. For planar electrodes, simulation results show that Li-ions can only transport vertically inside the tortuous electrode and reach the reaction sites from the top to the bottom (Fig. 2(a)). While for 3D grid porous electrodes, Li-ions may optionally go down through the vertically aligned pores, transversely get into the electrode, and then transport inside the electrode to reach the reaction sites (Fig. 2(e)). For the top part of the 3D grid electrodes, Li-ions mainly transport vertically inside the electrodes since the top part is close to the Li-foil. While for the bottom part, Li-ions mainly transport vertically through the macro-pores, and then transversely get into the electrode to reach the reaction sites. Figures 2(b)–2(d) and 2(f)–2(h) show the Li-ion concentration contour of planar electrodes and 3D grid porous electrodes at the end of discharge with the rate of 1.0, 2.0, and 5.0 C. It clearly shows that 3D grid porous electrodes enable more active materials involved in the electrochemical reactions than planar electrodes. This leads to increased specific capacities at various discharge rates (Fig. S4 in the ESM). The specific capacities at 1.0, 2.0, and 5.0 C increase from 99.6, 49.9, and 9.1 to 150.8, 98.9, and 25.8 $mAh \cdot g^{-1}$, respectively. These results verify the effectiveness of 3D grid porous electrodes in improving the reaction kinetics and electrochemical performance.

Furthermore, the effects of electrode porosity ε, active material particle d, electrode thickness h, electrode electronic conductivity σ_e, line width s_l, and pore size s_p on the electrochemical performance were systematically evaluated. Firstly, increasing porosity has positive effects on improving the specific capacities at high discharge rates (Fig. 3(a) and Fig. S5 in the ESM). As for the 0.3 mm thick grid porous electrodes,

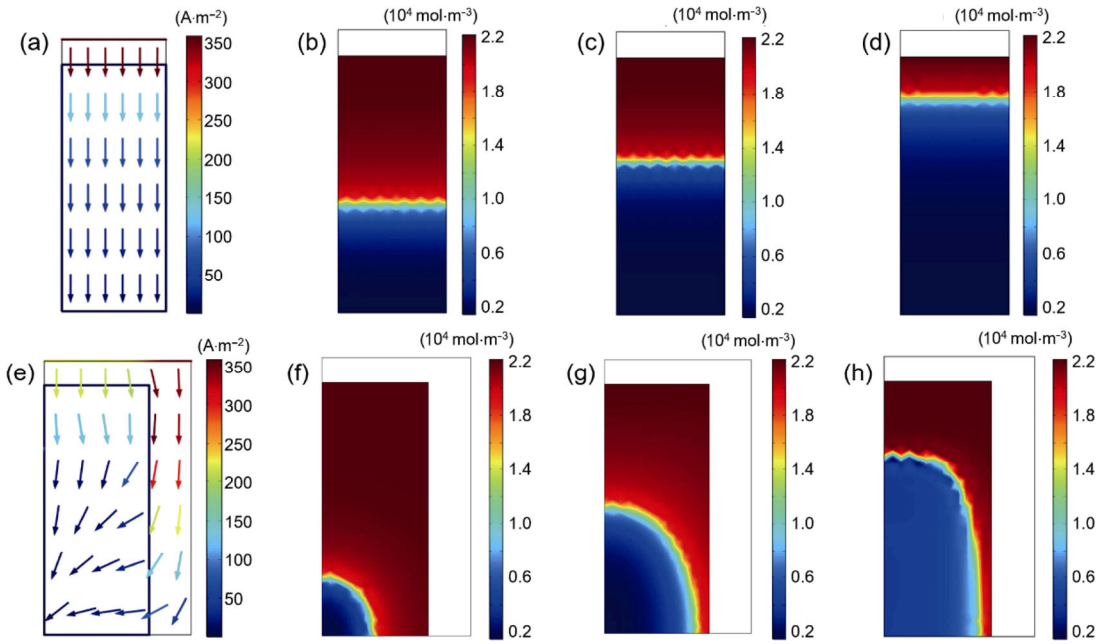

Fig. 2 Comparison of planar thick electrodes without vertical path and 3D grid porous thick electrodes with vertical path. (a) Electrolyte current density and direction for 0.3 mm planar thick electrodes; (b–d) Li-ion concentration at the end of discharge at 1.0, 2.0, and 5.0 C for 0.3 mm planar thick electrodes, respectively. (e) Electrolyte current density and direction for 0.3 mm 3D grid porous electrodes, respectively; (f–h) Li-ion concentration at the end of, respectively discharge at 1.0, 2.0, and 5.0 C for 0.3 mm 3D grid porous electrodes, respectively.

the specific capacity at 5.0 C increases from 25.8 to 97.1 mAh·g^{-1} when the porosity increases from 45% to 65%. To be noted, the actual porosity of 3D electrodes fabricated by low temperature direct writing was between 60% and 70%; thereby, the porosity of 65% was selected.

Secondly, reducing the active material particle diameter is also helpful for improving the specific capacity due to enhanced Li-ion transport in the solid phase (Fig. 3(b) and Fig. S6 in the ESM). As for the 0.3 mm thick grid porous electrodes, the specific capacity at 5.0 C increases from 25.8 to 49.2 mAh·g^{-1} when the particle diameter decreases from 10 to 2 μm. However, when the particle diameter reduces to less than 2 μm, further reduction seems to have little impact on the electrochemical performance. By simultaneously increasing porosity to 65% and reducing particle diameter to 2 μm, an impressive specific capacity of over 130 mAh·g^{-1}@5.0 C can be achieved for 0.3 mm thick grid porous electrodes (Fig. 3(c)). As for the electrode electronic conductivity, it has little effect on the electrochemical performance when it is over 10 S·m^{-1} (Fig. 3(c) and Fig. S7 in the ESM). However, poor electronic conductivity shall result in remarkable deterioration of performance if it is below 1.0 S·m^{-1}.

Although the synergistic effect of simultaneously increasing porosity to 65% and reducing active material particle diameter to 2 μm achieved excellent results for 0.3 mm thick 3D grid porous electrodes, it is not enough to overcome the charge delivery limitations at high charge/discharge rates with the further increase of electrode thickness to 0.6 mm or above (Fig. 3(d) and Fig. S8 in the ESM). For example, the specific capacity at 5.0 C decreases from over 130 mAh·g^{-1} to less than 50 mAh·g^{-1} when the electrode thickness increases from 0.3 to 0.6 mm.

Reducing line width is also beneficial for the improvement of electrochemical performance due to the reduction of Li-ion transport distance inside the electrode, but the improvement is not evident at high charge/discharge rates (Fig. 3(e) and Fig. S9 in the ESM). In addition, reducing pore size is found to have slight adverse effect on the high charge/discharge rate performance, possibly due to reduced electrolytes resulted from smaller pore size (Fig. 3(f) and Fig. S10 in the ESM).

To sum up, the electrochemical performance of 3D grid porous electrodes is influenced by many factors including electrode porosity, active material particle diameter, electronic conductivity, electrode thickness, line width, and pore size. These factors play different

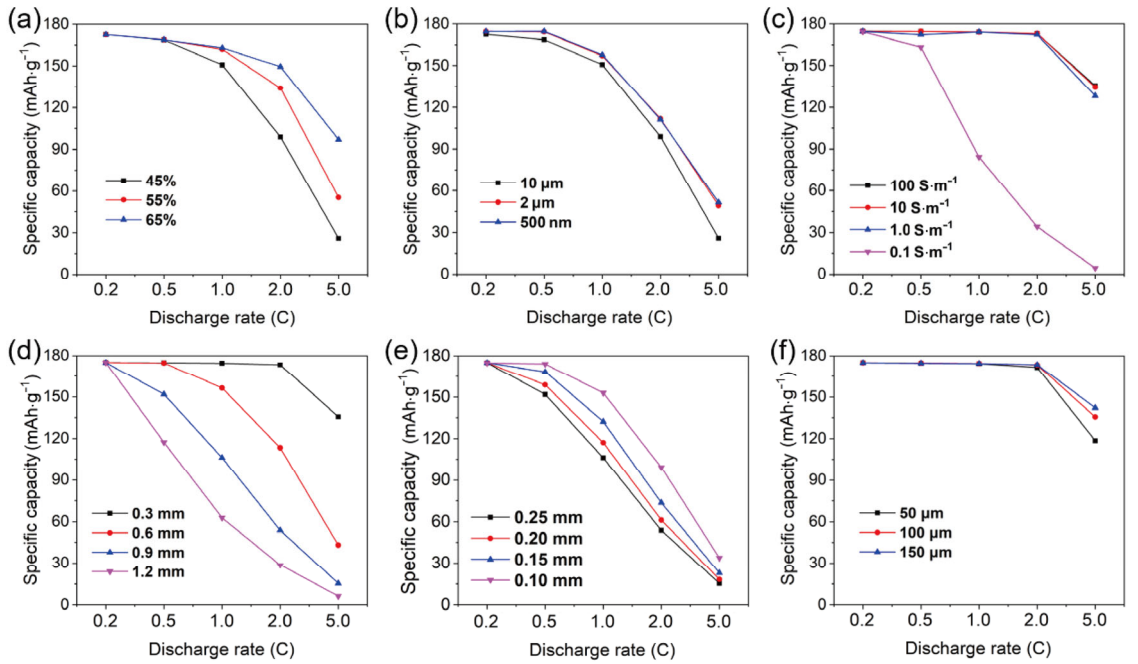

Fig. 3 Effects of various electrode parameters on the electrochemical performance: (a) specific capacity variation with discharge rate for 0.3 mm thick 3D grid porous electrodes with different porosities (d: 10 μm), (b) specific capacity variation with discharge rate for 0.3 mm thick 3D grid porous electrodes with different active material particle diameters (ε: 45%), (c) specific capacity variation with discharge rate for 0.3 mm thick 3D grid porous electrodes with different electronic conductivities (ε: 65%, d: 2 μm), (d) specific capacity variation with discharge rate for 3D grid porous electrodes with different thicknesses (ε: 65%, d: 2 μm), (e) specific capacity variation with discharge rate for 0.9 mm thick 3D grid porous electrodes with different line widths (ε: 65%, d: 2 μm), and (f) specific capacity variation with discharge rate for 0.3 mm thick 3D grid porous electrodes with different pore sizes (ε: 65%, d: 2 μm).

roles and impact the electrochemical performance at different levels. To eventually obtain 3D grid porous thick electrodes with excellent electrochemical performance, it is very important to determine the design guidelines based on the comprehensive understanding of the relationship between various influencing factors and electrochemical performance.

4 Experimental

To verify the results obtained with numerical simulation, we fabricated 3D grid porous LTO electrodes via a low temperature direct writing-based 3D printing process. Then we experimentally investigated the influence of various factors on electrochemical performance. Through the combination of simulation results and experimental results, a comprehensive understanding of the strength and weakness of 3D grid porous electrodes was obtained. Then basic guidelines for designing 3D grid porous electrodes with excellent electrochemical performance were proposed.

4.1 Ink preparation

To successfully maintain the shape during the printing process, ink properties, especially rheological properties are very important. Meanwhile, it is essential that the printed electrodes have excellent electronic conductivity so that efficient transport of electrons can be realized. In this study, we used highly conductive Ketjen black (KB; median diameter D_{50}: 30 nm, purchased from MTI Co., Ltd., Shenzhen, China) and multi-walled CNTs (MWCNTs; diameter: 8–15 nm, length: ~50 μm, purchased from XFNano Co., Ltd., Nanjing, China) to construct a hybrid conductive network in the electrodes to improve the electronic conductivity (Fig. S11 in the ESM). In this hybrid conductive network, KB particles form short-range conductive pathways and one-dimensional (1D) MWCNTs form long-range conductive pathways.

Firstly, MWCNT was dispersed into a mixed solvent composed of deionized water and 1,4-dioxane by ultrasonic dispersing with MWCNT concentration of 2.5 wt% to obtain a well-dispersed MWCNT solution.

The ratio of deionized water to 1,4-dioxane was 3:1. Then the mixed powder of LTO (purchased from MTI Co., Ltd., Shenzhen, China) and KB was balled milled for 12 h. 1.5 wt% binder, carboxymethyl cellulose (CMC; purchased from MTI Co., Ltd., Shenzhen, China), was added to MWCNT solution and magnetically stirred for 24 h. Then LTO/KB mixed powder was dispersed into the CMC/MWCNTs solution with a vacuum mixer to obtain a homogeneous ink. After that, the ink was filtered with a screen mesh to remove large clusters. The total solid content of LTO powder, KB, and MWCNTs was 40 wt%. The ink composition is shown in Table S2 in the ESM and the content of LTO:KB:MWCNTs was 6.17 g : 0.25 g : 0.25 g. To obtain an ink with the optimal electronic conductivity, we prepared inks with different ratios of KB and MWCNTs. Then the variation of electronic conductivity with conductive agent content was measured with a four-point probe machine (HPS2661, Helpass Technology, Co., Changzhou, China). Based on the electronic conductivity, the optimal ink composition was determined.

4. 2 Fabrication

The prepared LTO ink was loaded into a syringe and extruded through a nozzle with the diameter of ~210 μm in a low temperature chamber (−20 ℃) and frozen to form 3D grid porous electrodes. Then the electrodes were freeze-dried to remove solvents using a vacuum freeze-drying machine (FreeZone 4.5, Labconco Co., Ltd., USA). With this technology, highly porous electrodes with the porosity of up to 60%–70% can be obtained. The printed 3D grid porous electrodes were assembled into coin cell (CR2450) with Li-foil as the counter electrode. In this process, 0.5 mm thick foam copper and Celgard 2400 separators (purchased from MTI Co., Ltd., Shenzhen, China) were used to assemble the coin cells.

4. 3 Characterization

The electrode electronic conductivity was measured with a four-point probe machine. The rheological properties of LTO ink were measured on a commercial rheometer (MCR 702, Anton Paar GmbH, Graz, Austria). The size distribution of LTO active material was measured with a laser particle sizer (ZEN3690, Malvern Panalytical, Malvern, UK). The microstructures were characterized by the optical microscope (VHX-5000, Keygence, Osaka, Japan) and the scanning electron microscope (SEM; Supra55 Sapphire, Carl Zeiss, Oberkochen, Germany). The compressive mechanical properties of printed 3D grid porous electrodes were measured on a material testing machine (ElectroPuls E1000, Instron, Boston, USA). The porosity, pore size, and distribution were measured by mercury porosimetry (AutoPore lV9510, Micromeritics, Norcross, GA, USA). Electrochemical performance including the charge/discharge, rate capacities, and cycling performance was measured by an LAND test system (CT2001, LANHE, Wuhan, China).

4. 4 Results and discussion

The variation of electronic conductivity with conductive agent content is shown in Fig. S12 in the ESM. The intrinsic electronic conductivity of LTO is very low (~10^{-11} S·m^{-1}). While carbon conductive agents have very high electronic conductivity. The compressed disk of pure KB, MWCNTs, and acetylene black had an electronic conductivity of 651, 417, and 168 S·m^{-1}, respectively. By percolating LTO with different ratios of conductive agents, the electronic conductivity was improved to 0.1–36 S·m^{-1}. Results show that LTO/KB/MWCNT composite electrode containing hybrid conductive network has much higher electronic conductivity than LTO/KB electrode. This indicates that more effective transport of electrons can be obtained through this hybrid conductive network. In this study, a total content of 7.5 wt% with the ratio of KB:MWCNTs = 1:1 was selected due to its excellent electronic conductivity (22.73 S·m^{-1}) and relatively low mass ratio.

In addition to electronic conductivity, ink rheological properties are also very important. Apparent viscosity η_{app} decreases with the increase of shear rate exhibiting notable shear-thinning characteristics that is essential for 3D printing (Fig. 4(c)). η_{app} values of printable inks are in the same range as our previous study [54]. The storage modulus G' is larger than the loss modulus G'' when the shear stress is below the intersection point of two curves, indicating that the prepared ink exhibits solid-like characteristics at low shear stress (Fig. 4(c)). Meanwhile, when the shear stress is beyond the intersection point, G'' is larger than G', indicating that the ink exhibits liquid-like characteristics at high shear stress. This feature enables the ink flow through the syringe nozzle like liquid when external pressure is applied and maintain its shape like solid when external

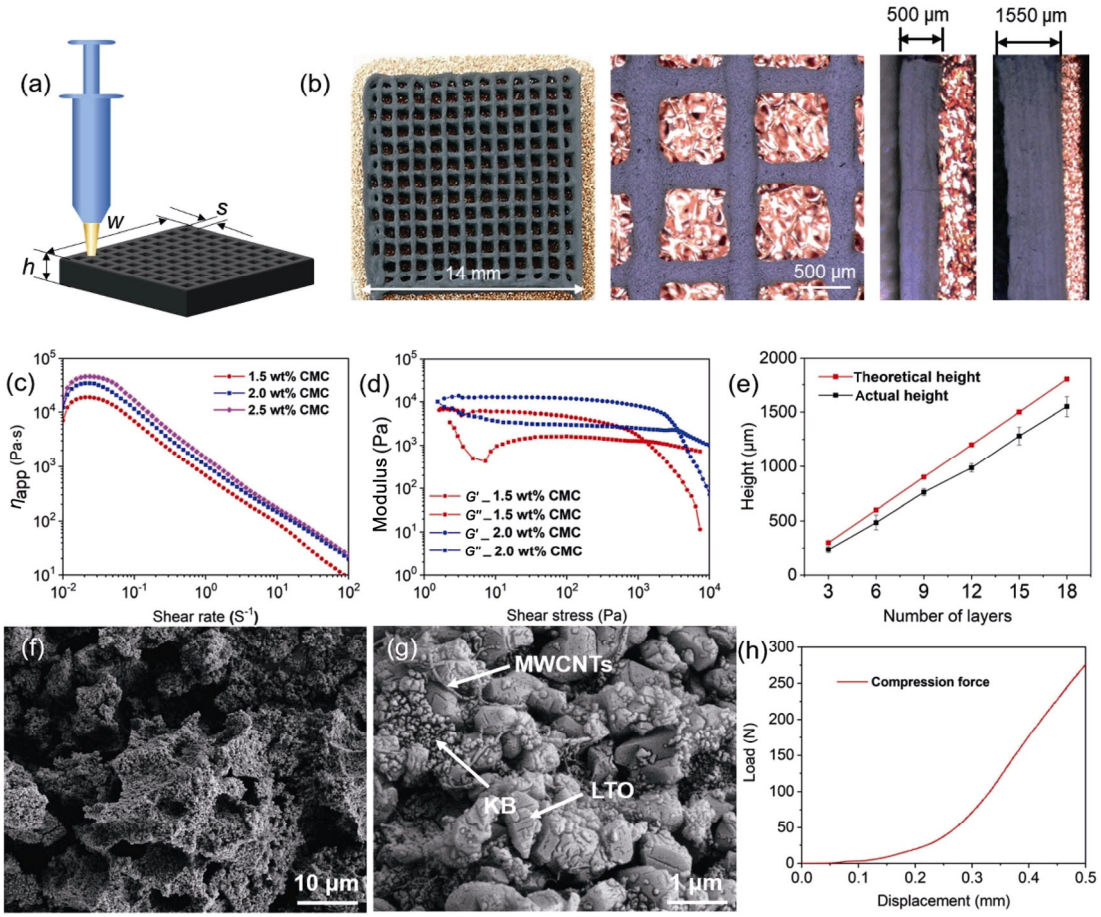

Fig. 4 Morphologies, ink rheological properties, microstructures, and compressive strength of 3D printed grid porous electrodes: (a) schematic of the printing process; (b) top view, magnified top view, and side view of the electrodes; (c) variation of apparent viscosity with shear rate; (d) storage modulus G' and loss modulus G''; (e) variation of electrode height with number of layers; (f, g) SEM microstructures; and (h) compressive behavior of printed electrodes with 18 layers.

pressure is removed once it is deposited onto the building plate. In this study, 1.5 wt% CMC concentration was selected. Based on the electronic conductivity and rheological properties, the final ink composition with the total solid content of ~40 wt% is listed in Table S2 in the ESM.

Once the ink was prepared, the next step was to optimize the printing process. The major printing parameters include: extrusion speed v_j, scanning speed v_s, and layer thickness h_s. The process was optimized with L9(3×3) orthogonal experiments. Processing parameters and fabrication results are listed in Table S3 and Fig. S13 in the ESM, respectively. 3D grid porous electrodes with the dimensions of 14 mm × 14 mm were fabricated. The top view, magnified top view, and side view of the electrodes are shown in Fig. 4(b). With the nozzle diameter of 210 μm, the line width of printed electrodes is about 294 μm. The actual height of printed electrodes was measured and plotted in Fig. 4(e). Results show that the actual height is about 85% of the theoretical height. Although some height reduction was observed, the printed electrodes were able to successfully maintain its shape during the printing process.

The particle size distribution of LTO powder is shown in Fig. S14 in the ESM. The average particle size was 409.5 nm with two peaks of 409 nm and 5.208 μm. Most of the particles were below 1 μm. The SEM images of 3D printed grid porous electrodes are shown in Figs. 4(f) and 4(g). MWCNT chains and KB particles are observed in the electrodes and form combined short-range and long-range hybrid conductive network. The compressive properties of electrodes with 18 layers show that 3D printed electrodes have excellent mechanical properties (Fig. 4(h)). They did not crush when the height reduced over 25% and the compression force was over 200 N. The excellent mechanical properties are beneficial to the long-term use of these 3D grid porous electrodes.

Porosity, pore size, and distribution were characterized by mercury porosimetry. The mercury intrusion pressure ranged from 3.64×10^{-3} MPa to 378 MPa corresponding to the pore size of 345 μm to 3.45 nm. The cumulative pore volume versus pressure and incremental pore volume versus pressure are shown in Fig. 5(a). The pore size distribution is shown in Fig. 5(b). Three peaks of pore size with the size range of 50–200 nm, 2–10 μm, and 100–200 μm are observed indicating that hierarchically porous structures were obtained in the electrodes. The measured porosity was 71.85%. To be noted, the porosity, pore size, and pore size distribution do not include the vertically aligned macro-pores formed by the space between the active material lines.

3D grid porous LTO electrodes with 4 layers, 8 layers, and 12 layers were fabricated. The corresponding thickness is ~350, ~760, and ~1085 μm and the areal mass loading is 12.89, 26.36, and 39.44 $mg\cdot cm^{-2}$, respectively. The charge/discharge curves at rates from 0.2 to 5.0 C were measured with the cut-off voltage of 2.5 and 1.0 V as shown in Figs. 6(a)–6(c). It can be seen that at low discharge rates of 0.2, 0.5, and 1.0 C, the discharge capacities are able to reach ~150 $mAh\cdot g^{-1}$ or above even for electrodes with the thickness of over 1 mm. When the discharge rate increases to 5.0 C, 4-layer electrode exhibits an impressive specific capacity of ~120 $mAh\cdot g^{-1}$. With the increase of electrode thickness, the discharge specific capacity at 5.0 C decreases sharply to less than 20 $mAh\cdot g^{-1}$. These experimental results are consistent with simulation results. This indicated that electrode thickness has huge impacts on the electrochemical performance at high discharge rates over 2.0 C. However, it is worth noting that even for electrodes with the thickness of 1085 μm, the specific capacity at 1.0 C is able to maintain above an impressive value of 145 $mAh\cdot g^{-1}$. The specific capacities at rates of below 1.0 C of all thick electrodes are comparable to conventional coated thin electrodes [53]. However, at high discharge rates of over 2.0 C, the specific capacities of 8-layer electrode and 12-layer electrode are lower than coated ones.

The variation of areal capacity with discharge rates is shown in Fig. 6(c). In general, the areal capacity increases with the increase of electrode thickness. For the 4-layer electrode, the areal capacity is ~2 $mAh\cdot cm^{-2}$ and decreases slightly with the increase of discharge rate. When the thickness is 1085 μm, the areal capacity increases to 6.37 $mAh\cdot cm^{-2}$@0.2 C and 5.88 $mAh\cdot cm^{-2}$@1.0 C. These values are higher than the values of 4.8 $mAh\cdot cm^{-2}$@0.2 C and 3.6 $mAh\cdot cm^{-2}$@2.0 C reported in our previous study due to increased electrode thickness and higher areal mass loading [53]. In addition, Sotomayor *et al*. [55] reported a power extrusion moulding method to fabricate additive-free thick LTO electrodes with the thickness of 500 μm and areal capacity of 15.2 $mAh\cdot cm^{-2}$, but this value can only be achieved at a very low discharge rate of 1/24 C. For the 8-layer and 12-layer electrodes, the areal capacity decreases remarkably when the discharge rate is over 2.0 C. From the Ragone plot that characterizes the relationship between areal power density and areal energy density (Fig. 6(f)), it can be seen that the energy density decreases only slightly when the discharge rates are below 1.0 C indicating that the trade-off between energy density and power density can be largely alleviated with 3D grid porous electrodes. When the electrode thickness is 1085 μm, the power density and energy density at 1.0 C are 8.04 $mW\cdot cm^{-2}$ and 28.95 $J\cdot cm^{-2}$, respectively. These values are much higher than previously reported values (Fig. 6(f)) [25,39]. Howerver, when the discharge rate is over 2.0 C, the thick electrodes show serious decay of both energy density and power density. These results indicate that this type of 3D grid porous thick electrodes is suitable

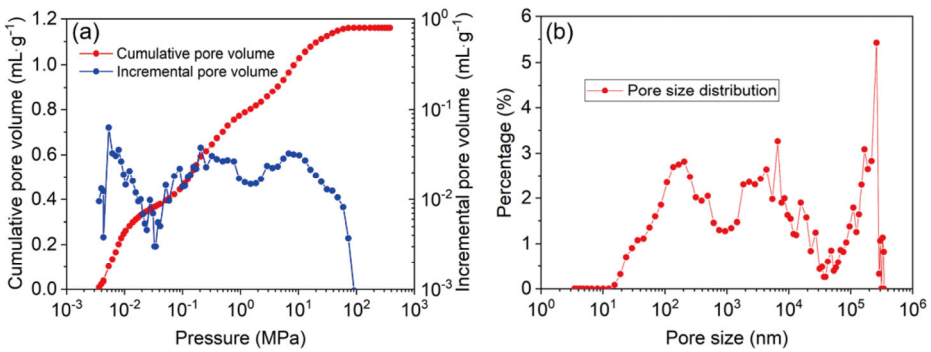

Fig. 5 Pore size and distribution of 3D printed grid porous electrodes: (a) cumulative and incremental pore volume versus pressure and (b) pore size distribution.

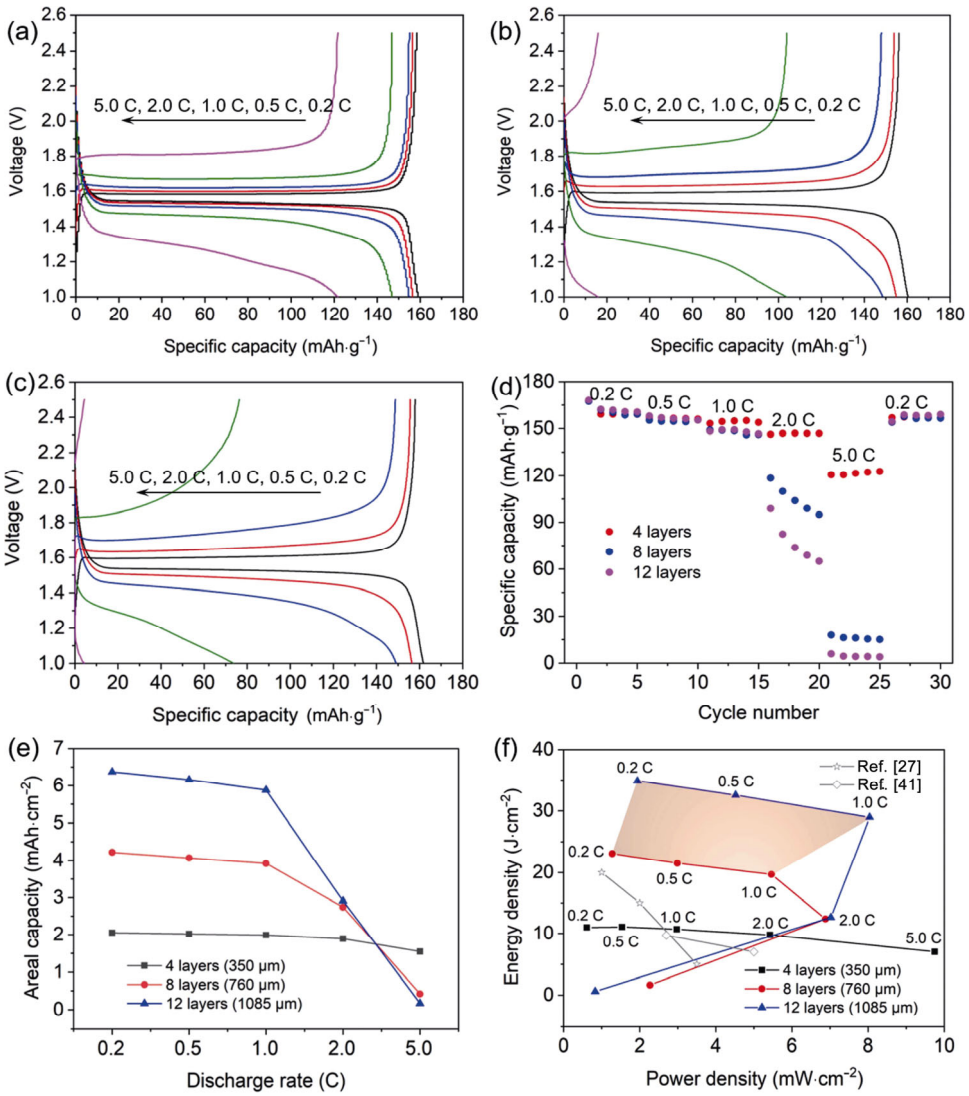

Fig. 6 Charge/discharge curves and rate capacities of electrodes with different thickness: (a) charge/discharge curves of electrodes with 4 layers, (b) charge/discharge curves of electrodes with 8 layers, (c) charge/discharge curves of electrodes with 12 layers, (d) rate performance, (e) areal capacity variation with discharge rate, and (f) Ragone plot of power density and energy density.

for those occasions that require high energy density but do not operate at high rates.

To evaluate the effects of line width on the electrochemical performance, 8-layer electrodes (electrode thickness: 760 μm) with the line width of 294, 266, and 220 μm were fabricated via 27, 30, and 32 G syringe needle, respectively (Figs. S15(a)–S15(c) in the ESM). The charge/discharge curves of electrodes with the line width of 294 μm are shown in Fig. S15(d) and the charge/discharge curves of electrodes with the line width of 266 and 220 μm are shown in Fig. S15(d) and Fig. S15(e) in the ESM. The comparison of rate performance is shown in Fig. S15(f) in the ESM. It can be seen that when the line width decreases to 220 μm, the specific capacity at 5.0 C increases from less than 20 to ~35 mAh·g^{-1}. The limited improvement suggests that reducing line width does not have significant effects on improving the electrochemical performance at high discharge rates for electrodes with the thickness of over 600 μm. This is consistent with simulation results.

To evaluate the effects of pore size on the electrochemical performance of 3D grid porous electrodes, 4-layer electrodes (electrode thickness: ~350 μm) with the pore size of 675, 460, and 269 μm were fabricated by varying the line spacing (0.1, 0.08, and 0.06 mm, respectively) (Figs. S16(a)–S16(c) in the ESM). The charge/discharge curves of electrodes are shown in

Figs. S16(d) and S16(e) in the ESM, respectively. The comparison of rate performance is shown in Fig. S16(f) in the ESM. It can be seen that when the discharge rate is below 1.0 C, the reduction of pore size has negligible effects on specific capacities. However, the specific capacity at 5.0 C declines with the reduction of pore size and this is in accordance with simulation results. Smaller pore size means reduced volume fraction of electrolyte and increased volume fraction of active materials, thereby resulting in the decline of specific capacity at high rates. Meanwhile, more evident reduction than simulation results is observed. The possible reason is that the 2D simulation model cannot completely reflect the effects of pore size on electrochemical performance for a 3D grid porous structure. However, it is worth noting that the specific capacity at 2.0 C remains above 120 $mAh \cdot g^{-1}$ even when the pore size reduces to 269 μm.

The cycling performance of the 4-layer electrode, 8-layer electrode, and 12-layer electrode was also measured with 100 cycles at 1.0 C (Figs. S17–S19 in the ESM). Results show that all electrodes exhibit nearly 100% coulombic efficiency. After 100 cycles, the specific capacity of 4-layer electrode is able to maintain ~145 $mAh \cdot g^{-1}$ and no capacity fading is observed (Fig. S17 in the ESM). While for the 8-layer and 12-layer electrodes, the specific capacity decreases to ~131 and ~120 $mAh \cdot g^{-1}$, respectively, with the capacity retention rate of 84.8% and 82.6% after 100 cycles. These results indicate that the cycling performance might deteriorate with the increase of electrode thickness. The influence of electrode thickness on cycling performance still requires further investigation. In addition, mechanical integrity is crucial for the long-term use of 3D grid porous thick electrodes. As a result, the cells were disassembled after 100 cycles and the thick electrodes are shown in Fig. S20 in the ESM. Results show that these thick electrodes are able to maintain its initial shape and no breaking-off was observed after 100 cycles.

To be noted, the introduction of vertically aligned pores and increased porosity play a "double-edge sword" dual role. On the one hand, it has the potential to overcome the charge delivery limitations of thick electrodes and make it possible for the electrode thickness increase up to over 1 mm. On the other hand, it will undermine the volumetric density of active materials and damage energy density. This "double-edge sword" effect requires further investigation.

5 Conclusions

3D grid porous LTO electrodes with vertically aligned pores were investigated in this study. Firstly, the structure and charge delivery mechanism were discussed. Then numerical simulations were performed to systematically evaluate the effects of electrode porosity, active material particle diameter, electronic conductivity, electrode thickness, line width, and pore size on electrochemical performance. Afterward, 4-layer, 8-layer, and 12-layer electrodes with the thicknesses of ~350, ~760, and ~1085 μm, respectively, were fabricated via low temperature direct writing. Simulation and experimental results show that by introducing vertically aligned pores and increasing porosity, it is able to overcome the charge delivery limitations below 1.0 C. Even for 1085 μm thick electrodes, the specific capacity at 1.0 C can reach over 140 $mAh \cdot g^{-1}$. The results indicate that the trade-off between energy density and power density at charge/discharge rates of below 1.0 C can be largely alleviated with the introduction of 3D grid porous electrodes. However, when the discharge rate is over 2.0 C, these thick electrodes exhibit relatively serious decay of both energy density and power density. To conclude, this type of 3D grid porous thick electrodes is suitable for those occasions that require high energy density at charge/discharge rates of below 1.0 C, but not appropriate for those applications that operate at high discharge rates of over 2.0 C.

Acknowledgements

This work is supported by the National Natural Science Foundation of China (Nos. 51705334 and 51975384) and the Shenzhen Science & Technology Projects (Nos. JCYJ20180305125025855 and JCYJ20200109105618137).

Electronic Supplementary Material

Supplementary material is available in the online version of this article at https://doi.org/10.1007/s40145-021-0533-7.

References

[1] Wang S, Yang Y, Dong Y, *et al*. Recent progress in Ti-based nanocomposite anodes for lithium ion batteries. *J Adv Ceram* 2019, **8**: 1–18.

[2] Ferrari S, Loveridge M, Beattie SD, *et al*. Latest advances

in the manufacturing of 3D rechargeable lithium microbatteries. *J Power Sources* 2015, **286**: 25–46.

[3] Kuang Y, Chen C, Kirsch D, *et al*. Thick electrode batteries: Principles, opportunities, and challenges. *Adv Energy Mater* 2019, **9**: 1901457.

[4] Sun H, Zhu J, Baumann D, *et al*. Hierarchical 3D electrodes for electrochemical energy storage. *Nat Rev Mater* 2019, **4**: 45–60.

[5] Arthur TS, Bates DJ, Cirigliano N, *et al*. Three-dimensional electrodes and battery architectures. *MRS Bull* 2011, **36**: 523–531.

[6] Roberts M, Johns P, Owen J, *et al*. 3D lithium ion batteries—From fundamentals to fabrication. *J Mater Chem* 2011, **21**: 9876.

[7] Inoue G, Kawase M. Numerical and experimental evaluation of the relationship between porous electrode structure and effective conductivity of ions and electrons in lithium-ion batteries. *J Power Sources* 2017, **342**: 476–488.

[8] Danner T, Singh M, Hein S, *et al*. Thick electrodes for Li-ion batteries: A model based analysis. *J Power Sources* 2016, **334**: 191–201.

[9] Gao H, Wu Q, Hu Y, *et al*. Revealing the rate-limiting Li-ion diffusion pathway in ultrathick electrodes for Li-ion batteries. *J Phys Chem Lett* 2018, **9**: 5100–5104.

[10] Landi BJ, Ganter MJ, Cress CD, *et al*. Carbon nanotubes for lithium ion batteries. *Energy Environ Sci* 2009, **2**: 638.

[11] Wang K, Wu Y, Luo S, *et al*. Hybrid super-aligned carbon nanotube/carbon black conductive networks: A strategy to improve both electrical conductivity and capacity for lithium ion batteries. *J Power Sources* 2013, **233**: 209–215.

[12] Liu X, Peng H, Zhang Q, *et al*. Hierarchical carbon nanotube/carbon black scaffolds as short- and long-range electron pathways with superior Li-ion storage performance. *ACS Sustainable Chem Eng* 2014, **2**: 200–206.

[13] Sander JS, Erb RM, Li L, *et al*. High-performance battery electrodes via magnetic templating. *Nat Energy* 2016, **1**: 16099.

[14] Chen C, Xu S, Kuang Y, *et al*. Nature-inspired tri-pathway design enabling high-performance flexible Li–O_2 batteries. *Adv Energy Mater* 2019, **9**: 1802964.

[15] Du G, Zhou Y, Tian X, *et al*. High-performance 3D directional porous $LiFePO_4$/C materials synthesized by freeze casting. *Appl Surf Sci* 2018, **453**: 493–501.

[16] Long J, Dunn B, Rolison D, *et al*. Three-dimensional battery architectures. *Chem Rev* 2004, **104**: 4463–4492.

[17] Ambrosi A, Pumera M. 3D-printing technologies for electrochemical applications. *Chem Soc Rev* 2016, **45**: 2740–2755.

[18] Fu K, Yao Y, Dai J, *et al*. Progress in 3D printing of carbon materials for energy-related applications. *Adv Mater* 2017, **29**: 1603486.

[19] Ruiz-Morales JC, Tarancón A, Canales-Vázquez J, *et al*. Three dimensional printing of components and functional devices for energy and environmental applications. *Energy Environ Sci* 2017, **10**: 846–859.

[20] Tian X, Jin J, Yuan S, *et al*. Emerging 3D-printed electrochemical energy storage devices: A critical review. *Adv Energy Mater* 2017, **7**: 1700127.

[21] Wei M, Zhang F, Wang W, *et al*. 3D direct writing fabrication of electrodes for electrochemical storage devices. *J Power Sources* 2017, **354**: 134–147.

[22] Zhakeyev A, Wang P, Zhang L, *et al*. Additive manufacturing: Unlocking the evolution of energy materials. *Adv Sci* 2017, **4**: 1700187.

[23] Zhang F, Wei M, Viswanathan VV, *et al*. 3D printing technologies for electrochemical energy storage. *Nano Energy* 2017, **40**: 418–431.

[24] Zhu C, Liu T, Qian F, *et al*. 3D printed functional nanomaterials for electrochemical energy storage. *Nano Today* 2017, **15**: 107–120.

[25] Chang P, Mei H, Zhou S, *et al*. 3D printed electrochemical energy storage devices. *J Mater Chem A* 2019, **7**: 4230–4258.

[26] Zeng L, Li P, Yao Y, *et al*. Recent progresses of 3D printing technologies for structural energy storage devices. *Mater Today Nano* 2020, **12**: 100094.

[27] Sun K, Wei TS, Ahn BY, *et al*. 3D printing of interdigitated Li-ion microbattery architectures. *Adv Mater* 2013, **25**: 4539–4543.

[28] Fu K, Wang Y, Yan C, *et al*. Graphene oxide-based electrode inks for 3D-printed lithium-ion batteries. *Adv Mater* 2016, **28**: 2587–2594.

[29] Hu J, Jiang Y, Cui S, *et al*. 3D-printed cathodes of $LiMn_{1-x}Fe_xPO_4$ nanocrystals achieve both ultrahigh rate and high capacity for advanced lithium-ion battery. *Adv Energy Mater* 2016, **6**: 1600856.

[30] Kohlmeyer RR, Blake AJ, Hardin JO, *et al*. Composite batteries: A simple yet universal approach to 3D printable lithium-ion battery electrodes. *J Mater Chem A* 2016, **4**: 16856–16864.

[31] Li J, Leu MC, Panat R, *et al*. A hybrid three-dimensionally structured electrode for lithium-ion batteries via 3D printing. *Mater Des* 2017, **119**: 417–424.

[32] Wang Y, Chen C, Xie H, *et al*. 3D-printed all-fiber Li-ion battery toward wearable energy storage. *Adv Funct Mater* 2017, **27**: 1703140.

[33] Chen QM, Xu R, He ZT, *et al*. Printing 3D gel polymer electrolyte in lithium-ion microbattery using stereolithography. *J Electrochem Soc* 2017, **164**: A1852-A1857.

[34] Liu C, Cheng X, Li B, *et al*. Fabrication and characterization of 3D-printed highly-porous 3D $LiFePO_4$ electrodes by low temperature direct writing process. *Materials* 2017, **10**: 934.

[35] Rocha VG, Rocha VG, García-Tuñón E, *et al*. Multimaterial 3D printing of graphene-based electrodes for electrochemical energy storage using thermoresponsive inks. *ACS Appl Mater Interfaces* 2017, **10**: 37136–37145.

[36] Cheng M, Jiang YZ, Yao WT, *et al*. Elevated-temperature 3D printing of hybrid solid-state electrolyte for Li-ion batteries. *Adv Mater* 2018, **30**: 1800615.

[37] Lacey SD, Kirsch DJ, Li YJ, *et al*. Extrusion-based 3D printing of hierarchically porous advanced battery electrodes. *Adv Mater* 2018, **30**: 1705651.
[38] Park SH, Kaur M, Yun D, *et al*. Hierarchically designed electron paths in 3D printed energy storage devices. *Langmuir* 2018, **34**: 10897–10904.
[39] Reyes C, Somogyi R, Niu S, *et al*. 3D printing of a complete lithium ion battery with fused filament fabrication. *ACS Appl Energy Mater* 2018, **1**: 10.
[40] Wang J, Sun Q, Gao X, *et al*. Toward high areal energy and power density electrode for Li-ion batteries via optimized 3D printing approach. *ACS Appl Mater Interfaces* 2018, **10**: 39794–39801.
[41] Wei T, Ahn B, Grotto J, *et al*. 3D printing of customized Li-ion batteries with thick electrodes. *Adv Mater* 2018, **30**: 1703027.
[42] Zhang C, Shen K, Li B, *et al*. Continuously 3D printed quantum dot-based electrodes for lithium storage with ultrahigh capacities. *J Mater Chem A* 2018, **6**: 19960–19966.
[43] Cao D, Xing Y, Tantratian K, *et al*. 3D printed high-performance lithium metal microbatteries enabled by nanocellulose. *Adv Mater* 2019, **31**: 1807313.
[44] Deiner LJ, Bezerra CAG, Howell TG, *et al*. Digital printing of solid-state lithium-ion batteries. *Adv Eng Mater* 2019, **21**: 1900737.
[45] Yu X, Liu Y, Pham H, *et al*. Customizable nonplanar printing of lithium-ion batteries. *Adv Mater Technol* 2019, **4**: 1900645.
[46] Zhou L, Ning W, Wu C, *et al*. 3D-printed microelectrodes with a developed conductive network and hierarchical pores toward high areal capacity for microbatteries. *Adv Mater Technol* 2019, **4**: 1800402.
[47] Ashby DS, Choi CS, Edwards MA, *et al*. High-performance solid-state lithium-ion battery with mixed 2D and 3D electrodes. *ACS Appl Energy Mater* 2020, **3**: 8402–8409.
[48] Bao Y, Liu Y, Kuang Y, *et al*. 3D-printed highly deformable electrodes for flexible lithium ion batteries. *Energy Storage Mater* 2020, **33**: 55–61.
[49] Gao X, Yang X, Sun Q, *et al*. Converting a thick electrode into vertically aligned “thin electrodes” by 3D-printing for designing thickness independent Li–S cathode. *Energy Storage Mater* 2020, **24**: 682–688.
[50] Zhu Y, Li J, Saleh MS, *et al*. Towards high-performance Li-ion batteries via optimized three-dimensional micro-lattice electrode architectures. *J Power Sources* 2020, **476**: 228593.
[51] Gao W, Pumera M. 3D printed nanocarbon frameworks for Li-ion battery cathodes. *Adv Funct Mater* 2021, **31**: 2007285.
[52] Lyu ZY, Lim GJH, Koh JJ, *et al*. Design and manufacture of 3D-printed batteries. *Joule* 2021, **5**: 89–114.
[53] Liu C, Xu F, Liu Y, *et al*. High mass loading ultrathick porous $Li_4Ti_5O_{12}$ electrodes with improved areal capacity fabricated via low temperature direct writing. *Electrochimica Acta* 2019, **314**: 81–88.
[54] Wu X, Liang X, Zhang X, *et al*. Structural evolution of plasma sprayed amorphous $Li_4Ti_5O_{12}$ electrode and ceramic/polymer composite electrolyte during electrochemical cycle of quasi-solid-state lithium battery. *J Adv Ceram* 2021, **10**: 347–354.
[55] Sotomayor ME, de la Torre-Gamarra C, Bucheli W, *et al*. Additive-free $Li_4Ti_5O_{12}$ thick electrodes for Li-ion batteries with high electrochemical performance. *J Mater Chem A* 2018, **6**: 5952–5961.

Open Access This article is licensed under a Creative Commons Attribution 4.0 International License, which permits use, sharing, adaptation, distribution and reproduction in any medium or format, as long as you give appropriate credit to the original author(s) and the source, provide a link to the Creative Commons licence, and indicate if changes were made.

The images or other third party material in this article are included in the article’s Creative Commons licence, unless indicated otherwise in a credit line to the material. If material is not included in the article’s Creative Commons licence and your intended use is not permitted by statutory regulation or exceeds the permitted use, you will need to obtain permission directly from the copyright holder.

To view a copy of this licence, visit http://creativecommons.org/licenses/by/4.0/.